RSC Advances

PAPER

View Article Online
View Journal | View Issue

Cite this: *RSC Adv.*, 2020, **10**, 18315

Synthesis and characterization of $BiVO_4$ nanoparticles for environmental applications

M. Ganeshbabu,[a] N. Kannan,[a] P. Sundara Venkatesh,*[a] G. Paulraj,[b] K. Jeganathan[b] and D. MubarakAli[c]

Received 4th February 2020
Accepted 27th April 2020

DOI: 10.1039/d0ra01065k

rsc.li/rsc-advances

In the present study, a chemical precipitation method is adopted to synthesize bismuth vanadate nanoparticles. The calcination temperature dependent photocatalytic and antibacterial activities of $BiVO_4$ nanoparticles are examined. The structural analysis evidences the monoclinic phase of $BiVO_4$ nanoparticles, where the grain size increases with calcination temperature. Interestingly, $BiVO_4$ nanoparticles calcined at 400 °C exhibit superior photocatalytic behaviour against methylene blue dye ($K = 0.02169\ min^{-1}$) under natural solar irradiation, which exhibits good stability for up to three cycles. The evolution of antibacterial activity studies using a well diffusion assay suggest that the $BiVO_4$ nanoparticles calcined at 400 °C can act as an effective growth inhibitor of pathogenic Gram-negative (*P. aeruginosa* & *A. baumannii*) and Gram-positive bacteria (*S. aureus*).

1 Introduction

The rapid rise of industrialization and urbanization unfavourably engenders the pollution of our precious natural resources leading to acute health issues in human beings.[1] Notably, water pollution is one of the fatal causes of several infectious diseases such as cholera, typhoid, and dysentery. The release of untreated effluents from textile industries into water resources is a prime cause of pollution which adversely affects aquatic organisms[2] and results in discontinuity in marine life cycle. In this regard, numerous approaches such as reverse osmosis, ion exchange, solvent extraction and chlorination are employed to treat effluents in the water reservoirs removing the dye molecules.[3] However, they have failed to eradicate the microorganisms completely. To overcome this critical issue, nanomaterials have been considered as a suitable candidate in this field owing to their unique physical and chemical properties such as increased surface to volume ratio, high diffusivity, and excellent reactivity.[4,5] In particular, metal oxide nanoparticles (NPs) are identified as ideal candidates for degrading organic pollutants in contaminated water and effective destruction of pathogens.[6,7] Among the wide range of metal oxide NPs, titanium dioxide (TiO_2) is widely investigated in the fields of photocatalysis and antibacterial activity as the result of its remarkable physiochemical properties inclusive of stability and super non-toxicity. Nevertheless, the efficiency of TiO_2 based nanomaterials in the field of photocatalytic dye degradation applications is still far from satisfactory due to its wide energy gap of ~3.4 eV.[8,9] Therefore, as a natural choice of interest the narrow band gap semiconducting nanomaterials with promising chemical stability and non-toxic behaviour are explored to enhance the photocatalytic dye degradation performance of the metal oxide NPs. It is well known fact that the sun light on surface of the earth consists of ~50% near infrared (NIR), ~45% visible light and only ~5% ultraviolet (UV) light.[10]

Recently, bismuth vanadate ($BiVO_4$) NPs has attained widespread of research interest in various fields like photovoltaic, solar water splitting and photocatalytic dye degradation applications owing to potential n-type semiconducting nature with visible band gap of 2.4 eV, excellent photo-stability with resistance to photo-corrosion.[11–13] Generally, the photocatalytic materials are expected to be a good antibacterial agent owing to their feasibility for the generation of reactive active species. Further, for the future day to day device viability, the materials with multiple applications are preferred. In this regard, the $BiVO_4$ receives wide range of research attention since it is a non-toxic material for the human cells and at the same time, it has a potential to fight against the infectious bacteria.[14] In addition to that, if the materials to be a better photocatalyst, it needs to cover almost entire visible region of solar spectrum. The $BiVO_4$ possess the most required band position to harvest the visible region from solar illumination and also able to possess antibacterial activity. Therefore, we strongly believe that the $BiVO_4$ NPs will simultaneously purify the contaminated water whether it is contaminated by some infectious bacteria nor organic dye molecules and its high antibacterial activity will play a major role in the long term and repeated usage of photocatalytic $BiVO_4$ NPs for real-time water purification. Even though, only few

[a]*Nanomaterials Laboratory, Department of Physics, Sri S. Ramasamy Naidu Memorial College, Sattur-626 203, Tamilnadu, India. E-mail: srnmcphysics@gmail.com*
[b]*Centre for Nanoscience and Nanotechnology, Department of Physics, Bharathidasan University, Tiruchirappalli-620 024, Tamilnadu, India*
[c]*School of Life Sciences, B. S. Abdul Rahman Crescent Institute of Science and Technology, Chennai-600 048, Tamilnadu, India*

research works have been emerged in the field of antimicrobial studies of $BiVO_4$ NPs.[14–19] However, its antimicrobial efficiency is still for from satisfactory. Therefore, we are motivated to synthesis $BiVO_4$ NPs and study its antimicrobial efficacy and dye degradation performance.

In general, $BiVO_4$ exists in three distinct crystal phases, namely monoclinic scheelite (clinobisvanite), tetragonal zircon (dreyerite) and tetragonal scheelite (pucherite).[20,21] Among them, the monoclinic scheelite (clinobisvanite) phase of $BiVO_4$ is considered the most favourable photocatalyst for visible light driven dye degradation applications, as it offers relatively narrow band gap (<2.4 eV) than the tetragonal zircon (dreyerite) and tetragonal scheelite (pucherite) phases.[18,22] Consequently, numerous approaches have been adopted to synthesis high quality $BiVO_4$ NPs such as hydrothermal method,[23] sol–gel method,[5] microwave synthesis,[14] chemical precipitation and solvo-thermal method.[24] Among them, the traditional chemical precipitation method is adopted in this paper, since this is a simple, cost effective and surfactant free approach for the preparation of $BiVO_4$ NPs.

The synthesis of high quality $BiVO_4$ NPs using the traditional chemical precipitation approach was presented in the paper. The prepared samples were calcined at the temperatures of 400°, 500° and 600 °C for attaining better crystallinity. The structural and vibrational studies evidences that the NPs calcinated under 400 °C is more suitable for various applications. Subsequently, the photocatalytic and antibacterial activities of $BiVO_4$ NPs were tested with respect to various calcination temperatures. The photocatalytic results evidence that $BiVO_4$ NPs calcinated at 400 °C exhibits a superior degradation of methylene blue (MB) for about 92.25% within 120 min under natural sun light and also it retains the degradation stability up to 3 cycles.

1.1 Synthesis of $BiVO_4$ nanoparticles

All chemicals used were of analytical grade and were purchased from Sigma-Aldrich. They were used without further purification.

For the synthesis of $BiVO_4$ NPs by the chemical precipitation technique, bismuth nitrate pentahydrate [$(BiNO_3)_3 \cdot 5H_2O$], ammonium metavanadate (NH_4VO_3), nitric acid (HNO_3) and sodium hydroxide (NaOH) were used as precursors without further purifications. $(BiNO_3)_3 \cdot 5H_2O$ and NH_4VO_3 were dissolved in 1 M of HNO_3 solution with 1 : 1 molar ratio. Initially, a reddish yellow solution was obtained and to increase the pH value to 10, NaOH (1 M) solution was constantly added by dropwise under vigorous stirring for 1 hour. The resultant pale yellowish solution was centrifuged as well as washed with double distilled (DD) water for several times and the precipitate was dried and finely grained. This prepared $BiVO_4$ powder was then calcined in a muffle furnace at different temperatures (400 °C, 500 °C and 600 °C) for 1 hour.

The crystal structure of the $BiVO_4$ NPs was analysed with data from X-ray diffractometer (Bruker D8 Advance, Germany) with CuK_α radiation of wavelength $\lambda = 1.5406$ Å. The diffraction patterns were recorded using θ–2θ geometry between 10° and 80° with step size of 0.05° for the structural identification. The surface morphologies of $BiVO_4$ NPs were examined by a field emission scanning electron microscope (FESEM, Carl Zeiss-Σigma, Germany). Diffuse reflectance spectroscopy (DRS) was measured using UV-visible spectrophotometer (JASCO V-750, Japan). Raman spectra were obtained by confocal Raman microscopic systems (NT-MDT, Russia) with a 473 nm laser (spot size ~0.5 μm in diameter cobalt laser). Photoluminescence (PL) spectra were also recorded using the same system with the excitation wavelength of 325 nm.

1.2 Experimental details of photocatalytic activity

The decolourisation of methylene blue (MB) dye solution has been investigated using $BiVO_4$ NPs calcinated at different temperatures (400 °C, 500 °C & 600 °C) as photocatalyst. All the photocatalytic experiments were carried out using 50 mg of photocatalyst ($BiVO_4$ NPs) in 5 ppm of MB dye solution. The prepared colloidal solution was sonicated to attain complete dispersion of catalyst, and later it was kept under direct sunlight. This work was conducted on sunny day at Sattur, Tamil Nadu, India (geographical location of 9.37°N 77.93°E) between 2 pm to 4 pm. During the illumination, 5 ml of dye solution was taken at the equal intervals of 15 minutes from 0 up to 120 minutes. To examine the degradation of MB, the collected solutions were filtered and the UV-Vis absorption spectra were recorded by UV-visible spectrometer (JASCO V-760).

1.2.1 Radical trapping studies. The radical trapping studies were taken to make out the role of reactive species during the degradation process. For this analysis, benzoquinone (BQ), isopropyl alcohol and ethylene diamine tetra acetic acid (EDTA) were engaged as the scavengers for hydroxyl radical (OH), super oxide radical ($O_2^{\bullet -}$) and holes h^+ respectively.[1,25,26] The similar dye degradation procedure was adopted along with the scavenger of 1 mM of each with the photocatalyst.

1.3 Bacterial inactivation test

Antibacterial efficacy of the $BiVO_4$ NPs was studied against Gram-negative (*P. aeruginosa* and *A. baumannii*) and Gram-positive (*S. aureus*) pathogens by well-diffusion method. Briefly, 100 μl of bacterial suspension with turbidity of 0.5 McFarland units (1.5×10^8 colony-forming units per millimeter) was spread over Mueller–Hinton agar (MHA) plates under aseptic conditions and the wells were formed with cork borer. Each of the wells was filled with 100 μl of $BiVO_4$ NPs solution in the concentration of 200 mg ml^{-1}. The plates were incubated at 37 °C for 24 h.

2 Results and discussion

2.1 Structural and optical studies of $BiVO_4$ NPs

X-ray diffraction patterns of the $BiVO_4$ NPs calcinated at different temperatures are shown in Fig. 1. All the diffraction peaks in the XRD spectra are well in agreement with the JCPDS card no. 014-688 and corresponding to the monoclinic phase of $BiVO_4$ NPs. The grain size has been calculated using Scherer

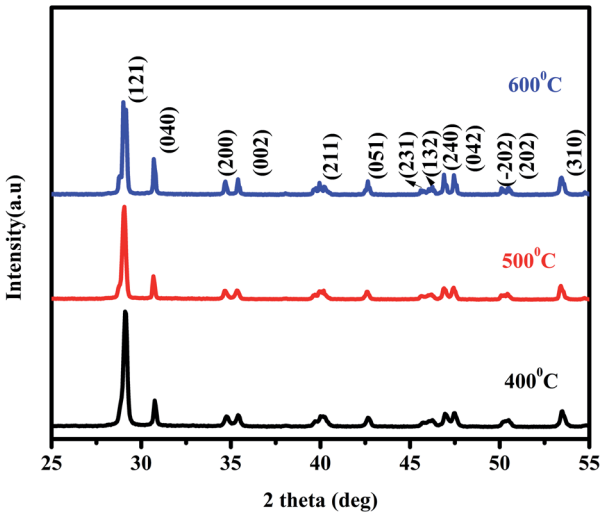

Fig. 1 XRD pattern of $BiVO_4$ NPs calcinated at different temperatures.

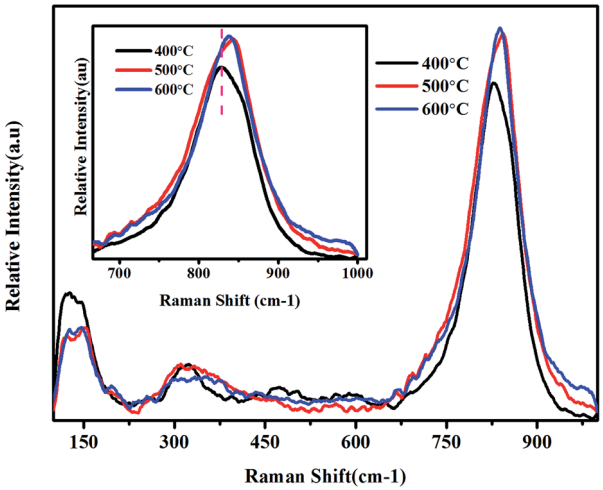

Fig. 2 Micro-Raman spectra of $BiVO_4$ NPs calcinated at different temperatures.

formula and its values are 34, 38 and 42 nm for the $BiVO_4$ NPs calcinated at 400, 500 & 600 °C respectively. The lattice parameters and volume of the unit cells of $BiVO_4$ NPs calcinated at different temperatures were evaluated using the following relations.

$$\frac{1}{d^2} = \frac{1}{\sin^2\beta}\left(\frac{h^2}{a^2} + \frac{k^2\sin^2\beta}{b^2} + \frac{l^2}{c^2} - \frac{2hl\cos\beta}{ac}\right) \quad (1)$$

$$V = abc\sin\beta \quad (2)$$

The obtained values for $BiVO_4$ NPs calcinated at different temperatures are given in Table 1. From the table, it is understood that the experimental results are in good agreement with the standard values of monoclinic $BiVO_4$.[27,28] An increase in calcination temperature leads to substantial increase in observed grain size. This may be attributed to the recrystallization and agglomeration of ultrafine grains.

Micro-Raman spectroscopy is a powerful tool to analyse the crystalline quality, phase orientation and transport properties of the materials. Raman spectra of $BiVO_4$ NPs calcinated at various temperatures are depicted in Fig. 2. The characteristic peak absorbed at 827 cm^{-1} for the $BiVO_4$ NPs calcinated at 400 °C, which corresponds to the symmetric stretching mode of V–O bonds.

This peak linearly exhibits blue shift with the calcination temperature, signifying a significant distortion in bond length with calcination temperature. The V–O bond length of the samples was calculated using the following empirical expression.[29]

$$\nu\ (cm^{-1}) = 21349\exp[1.917R\ (Å)] \quad (3)$$

where, ν is the Raman stretching frequency (cm^{-1}) and R is the bond length (Å). The calculated bond length for the $BiVO_4$ NPs calcinated at different temperatures is tabulated in Table 2.

This decrease in bond length may be attributed to the recrystallization of $BiVO_4$ NPs under high calcination temperature. The shoulder peak around at 688 cm^{-1} corresponds to the ν^3 antisymmetric stretching mode of VO_4. The Raman

Table 2 Variations of stretching frequency, V–O bond length and band gap of $BiVO_4$ NPs with respect to different calcination temperatures

Calcination temperature	Raman stretching frequency (cm^{-1})	Bond length (Å)	Band gap (eV)
400 °C	827	1.6956	2.28
500 °C	845	1.6846	2.36
600 °C	840	1.6873	2.38

Table 1 Lattice parameters and unit cell volume of $BiVO_4$ NPs calcinated at difference temperatures

Calcination temperature	a (Å)	b (Å)	c (Å)	β (degree)	Volume of the unit cell ($Å^3$)
JCPDS 00-014-0688	5.1950	11.7010	5.0920	90.38	309.52
400 °C	5.1670	11.6439	5.0732	90.10	305.220
500 °C	5.1783	12.6862	4.7873	90.37	314.558
600 °C	5.2028	12.9060	5.0806	94.37	340.155

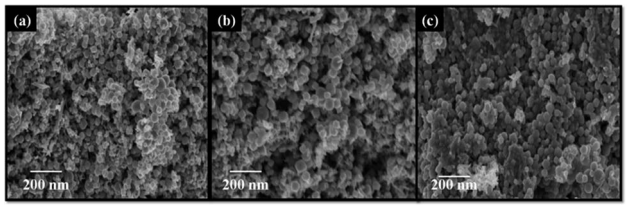

Fig. 3 FESEM images of the $BiVO_4$ NPs calcinated at different temperatures (a) 400 °C, (b) 500 °C and (c) 600 °C.

spectroscopy analysis evidences the formation of $BiVO_4$ NPs and corroborates with earlier reports.[21,30]

Fig. 3 shows the FESEM images of $BiVO_4$ NPs calcinated at different temperatures. For all the samples, the grains are found to be spherical in shape with high degree of uniformity, where the size distribution for 400, 500 & 600 °C are found to be are 154, 186 and 188 nm, respectively. The size of the $BiVO_4$ NPs gradually increases with the calcination temperature, which is in good agreement with XRD results. The increase in particle size may be attributed to the agglomeration of NPs at higher calcination temperature.

UV-visible diffuse reflectance spectra of $BiVO_4$ NPs different calcination temperatures are shown in Fig. 4(a). For the determination of band gap energy, Kubelka–Munk *vs.* energy plot is drawn using the following formula and shown in Fig. 4(b).

$$F(R) = \frac{(1-R)^2}{2R} \quad (4)$$

Here, R is the reflectance data of the prepared sample with respect to the wavelength. The band gap energy varies from 2.28 to 2.38 eV for the $BiVO_4$ NPs and represented in Table 2. A significant up-shift in the band gap of $BiVO_4$ NPs is observed with increase in the calcination temperature.

2.2 Photocatalytic dye degradation studies of $BiVO_4$ NPs

The photocatalytic performance of $BiVO_4$ NPs calcinated at different temperatures is examined by the degradation of MB dye molecules under natural solar light irradiation. The photocatalytic dye degradation performance graphs of $BiVO_4$ NPs calcinated at different temperatures is depicted in Fig. 5(a–c). From the spectra, it is perceived that the intensity of the characteristic peak of MB observed at 664 nm decreases with respect to the time for all the three samples.

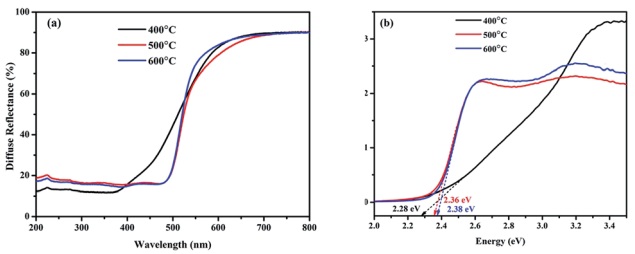

Fig. 4 UV-visible diffuse reflectance spectra of $BiVO_4$ NPs calcinated at different temperatures. (a) Reflectance spectra and (b) K–M *vs.* energy plot.

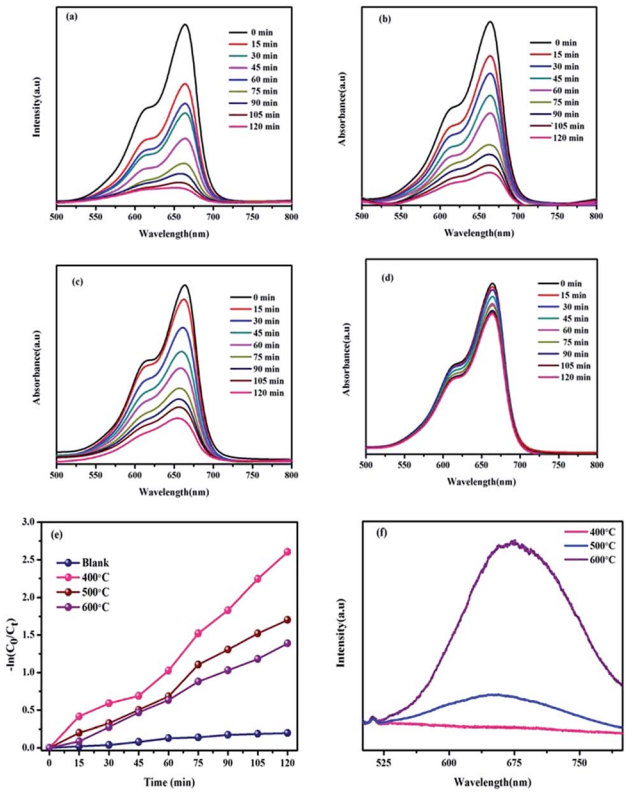

Fig. 5 Time dependent UV-Vis spectra for the photocatalytic degradation of MB using $BiVO_4$ NPs calcinated at different temperatures under solar irradiation (a) 400 °C (b) 500 °C (c) 600 °C (d) without catalyst (e) pseudo first order kinetic rate plot of $BiVO_4$ NPs with respect to irradiation time and (f) PL spectra of $BiVO_4$ NPs.

It is worth to note that the photocatalyst loaded dye solutions shows ~5 times greater as compared to the bare dye solution as shown in Fig. 5(d). In particular, $BiVO_4$ NPs calcinated at 400 °C exhibit superior photocatalytic performance of 92.25% degradation within 120 min. This exhibits better degradation percentage as compared to the $BiVO_4$ NPs calcinated at 500 °C (81.76%) and 600 °C (75.07%). The decrement of photocatalytic performance with calcination temperature is due to quick recombination of photo-excited electrons and holes, as further confirmed by normalized PL spectra of $BiVO_4$ NPs calcinated at various temperatures as shown in Fig. 5(f). Usually, the low and high intense peaks represent the low and high recombination rates respectively. In Fig. 5(f), it is noticed that the broad peak between 550 to 800 nm followed by the near band edge emission at 512 nm indicates the presence of defects in $BiVO_4$ NPs. The intensity of this peak increases with the calcination temperature indicating a fast charge recombination of photo-generated charge carriers (electrons and holes) with suppression the photocatalytic activity.[31–33] From the PL spectra, the $BiVO_4$ NPs calcinated at 400 °C is identified to support slower charge recombination, whose rate increases with the increasing calcination temperature towards 600 °C. Due to this, the

Table 3 Comparison of photocatalytic performance of $BiVO_4$ NPs calcinated at different temperatures

Type of sample	% of degradation	K (min^{-1})
Without catalyst	17.95	0.00164
$BiVO_4$ calcinated at 400 °C	92.50	0.02169
$BiVO_4$ calcinated at 500 °C	81.76	0.01418
$BiVO_4$ calcinated at 600 °C	75.07	0.01157

photocatalytic performance of $BiVO_4$ NPs decreases with calcination temperature.

The decomposition percentage of photocatalyst has been calculated using Beer–Lambert's law given below.

$$\text{Degradation percentage} = [1 - C_t/C_0] \times 100 \quad (5)$$

where, C_0 is the initial concentration of dye solution and C_t is the concentration of dye with respect to time t. The kinetic fit plot of $-\ln(C_t/C_0)$ *vs.* time is given in the Fig. 5(e). The pseudo first order rate constant (K) is calculated using the following relation and represented in Fig. 5(e).

$$-\ln(C_t/C_0) = Kt \quad (6)$$

For comparison, the catalyst free and calcinated $BiVO_4$ NPs loaded MB's degradation rate constant and percentage of degradation are given in the Table 3. When compared with binary and ternary composites, the single photocatalyst ($BiVO_4$ NPs calcinated at 400 °C) shows the highest first order kinetics (K) per minutes (0.0216 min^{-1}) as given in Table 4. This is a credential to $BiVO_4$ NPs for the practical applications.

Stability of the materials is a most important decisive factor for the good photocatalyst. For recycling studies, the best photocatalyst ($BiVO_4$ NPs calcinated at 400 °C) was chosen from the initial degradation results. After the successful completion of each cycle (120 min), the MB dye solution containing $BiVO_4$ NPs calcinated 400 °C was retrieved by removal of excess supernatant. This catalyst was added into a new dye solution and the dye degradation studies were carried out. Similarly, this process was continued up to three runs. The obtained results are presented in Fig. 6(a). From the recycling test, it is noticed that the photocatalytic dye degradation efficiency is slightly decreased from 92.25% (first cycle) to 85.65% (third cycle). This result validates that $BiVO_4$ NPs calcinated at 400 °C is having the appreciable stability even though the degraded product attached on the surface of photocatalyst.

2.3 Photocatalytic degradation mechanism of MB by $BiVO_4$ NPs

A schematic photocatalytic degradation mechanism of MB dye molecule by $BiVO_4$ is given in the Fig. 7. When the photon from the sun light fall on the surface of the $BiVO_4$ NPs, the electrons in the valence band get excited to conduction band by leaving a hole on

Table 4 Comparison of first order kinetics of $BiVO_4$ NPs calcinated at 400 °C with other reported photocatalysts

Photocatalyst	Light source	First order kinetics-K (min^{-1})	Ref.
P2SABSA modified TiO_2	1000 W xenon lamp (UV)	0.0138	34
TiO_2/Ag/SnO_2 (2 wt%)	500 W xenon lamp (UV)	0.0190	35
CdS–CuS	250 W tungsten lamp (visible light)	0.0090	36
ZnO : Cr 1%	Direct sun light	0.0153	37
ZnO/SnO_2	Direct sun light	0.0120	38
α-Fe_2O_3/Fe_2O_3	160 W mercury lamp	0.0100	39
Bentonite/g-C_3N_4	300 W xenon lamp	0.0123	40
Zno-RGO	300 W mercury lamp	0.0172	41
$BiVO_4$ calcinated at 400 °C	**Direct sun light**	**0.0216**	**Present work**

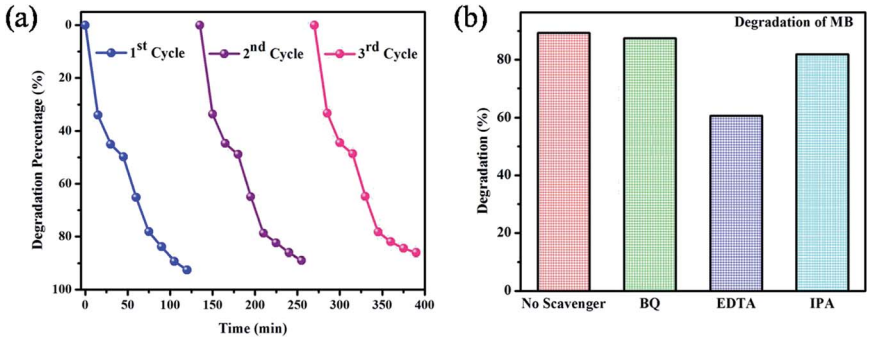

Fig. 6 (a) The photocatalytic stability of $BiVO_4$ NPs calcinated at 400 °C (b) effect of scavengers on the degradation of MB.

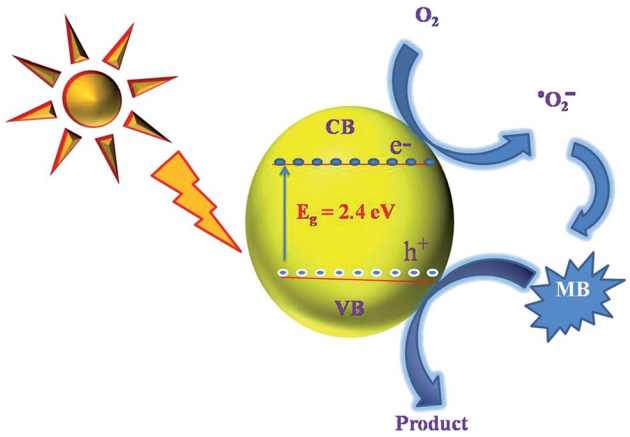

Fig. 7 A pictorial representation of photocatalytic dye degradation mechanism for MB by $BiVO_4$ NPs.

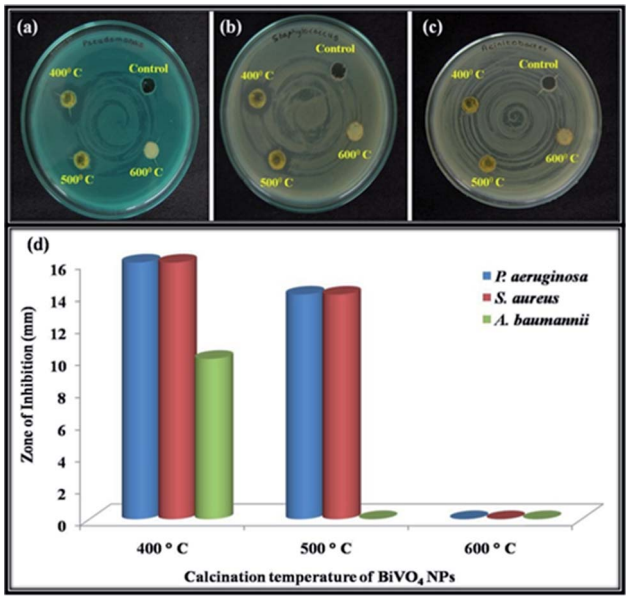

Fig. 8 Well diffusion assay photographs of $BiVO_4$ NPs calcinated at different temperatures (400–600 °C) on the clinical pathogens showing antibacterial effects against (a) *P. aeruginosa* (b) *S. aureus* (c) *A. baumannii* (d) antibacterial efficacy.

the valence band. These photo-generated holes (h^+) readily react with the adsorbed water molecules resulting in highly reactive hydroxyl radical (OH^-). At the same time, the electrons in the conduction band reacts with dissolved oxygen in the dye solution to generate superoxide anion radicals (O_2^-). These reactive species (OH^- & O_2^-) can degrade MB dye into non-toxic organic compounds. In this way, $BiVO_4$ NPs act as a potential photocatalyst for the degradation of MB dye molecules. To elucidate these phenomena, the radical trapping study was performed and the experiment results signify the percentage of degradation is in the order of EDTA < IPA < BQ < no scavenger. EDTA (h^+ scavenger) added solution shows lesser degradation as compared to no scavenger added solution. It means that the EDTA hunts the photo-generated holes and therefore, the EDTA added scavenger solution results poor dye degradation. From this analysis, it was confirmed that holes (h^+) are the major contributors in the photocatalytic degradation process. In a similar manner, the IPA and BQ are scavengers of hydroxyl and super oxide radicals, respectively with a role in photo degradation process. From the scavenger analysis, it is concluded that the role of IPA and BQ is relatively less as compared to EDTA.[1,25,26]

2.4 Antibacterial studies of $BiVO_4$ NPs

The digital image of bactericidal studies of the $BiVO_4$ NPs calcined at 400 °C shows the maximum inhibition (16 mm) on Gram-negative bacterium (*P. aeruginosa*) within 24 h. On the other hand, the same sample takes 48 h to inhibit the Gram-positive bacteria (*S. aureus*). The time delay for the inhibition of Gram-positive bacteria is due to the relatively thick cell wall to that of Gram-negative bacterium.[42] The $BiVO_4$ NPs calcinated at 400 °C exhibit inhibition of 10 mm against *A. baumannii* in the time interval of 24 h, even though the *A. baumannii* having the multi drug resistance.[43] On the same time, $BiVO_4$ NPs calcinated at 500 °C inhibits up to 14 mm against *P. aeruginosa* & *S. aureus* but not showed any activity against *A. baumannii*. In the case of $BiVO_4$ NPs calcinated at 600 °C, the anti-bacterial activity was not observed (Fig. 8).

2.5 Antibacterial mechanism of $BiVO_4$ NPs

Antibacterial action of NPs is a complex reaction which happens either on the cell wall or inside the intercellular organelles of

Table 5 Comparison of zone of inhibition capability of $BiVO_4$ NPs with previously reported antibacterial studies

Pathogenic bacteria	Materials	Zone of inhibition (mm)	Ref.
S. aureus	$Ag_2O \cdot CeO_2 \cdot ZnO$	11	45
	$NiO \cdot CeO_2 \cdot ZnO$	14	46
	Pind/Ag–Co_3O_4	10	47
	$BiVO_4$ calcinated at 400 °C	**16**	**Present work**
P. aeruginosa	$Ag_2O \cdot CeO_2 \cdot ZnO$	11	46
	$NiO \cdot CeO_2 \cdot ZnO$	13	45
	$BiVO_4$ calcinated at 400 °C	**16**	**Present work**
A. baumannii	17 type of commonly used antibiotics	6	43
	Levofloxacin	10	43
	Minocycline	10	43
	$BiVO_4$ calcinated at 400 °C	**10**	**Present work**

the pathogenic bacteria. Usually the NPs inhibits the bacteria in such a way that (i) damages the cell wall of bacteria, (ii) interrupts the replication of DNA and formation of reactive oxygen species (ROS), (iii) inhibits the protein production and (iv) disrupts the metabolism of the bacterium.[44] The size and formation of ROS (h^+, $^{\bullet}O_2^-$ & OH^-) are the most important criteria for the inhibition of pathogenic bacteria. The size of the bacteria generally is in the order of micrometre and the cell wall is permeable to tiny mono-dispersed NPs. In present case, $BiVO_4$ NPs calcinated at 400 °C is having small crystallite size with good mono-dispersion as compared to the other calcined samples, evident from XRD and SEM analysis. This may be attributed for the high antibacterial activity against Gram positive and negative bacteria. Additionally, the reactive species formation is also high for the 400 °C calcinated samples (from photocatalytic studies). However, the exact role of $BiVO_4$ NPs on the antibacterial activity is yet to be understood clearly.

Table 5 is suggesting that the $BiVO_4$ NPs calcinated at 400 °C is having the superior antibacterial activity as compared to the ternary nanocomposites. Most specifically, the inhibition of *A. baumannii* is comparatively high as compared to the commercially available 17 antibiotics. Among them, the inhibition zone is equal for highly toxic and costliest antibiotics such as levofloxacin and minocycline. This result suggests the alternate to the aforementioned antibiotics

3 Conclusion

The effect of calcination temperature on the structural, optical, photocatalytic and antibacterial behaviours of $BiVO_4$ NPs is investigated with proper mechanism. The structural studies reveal the monoclinic scheelite phase of $BiVO_4$ NPs. The grain size increases with the calcination temperature of NPs, where the morphological and elemental studies confirm the uniformity of spherical shaped grains and purity of $BiVO_4$ NPs. The $BiVO_4$ NPs calcinated at 400 °C manifests a great degradation of MB dye at about 92.25% within 120 min under natural sun light. Interestingly, the $BiVO_4$ NPs retain its degradation stability upto 3 cycles. Additionally, the $BiVO_4$ NPs calcinated at 400 °C could acts as a potential inhibitor to the growth of highly infectious bacteria (*S. aureus*, *P. aeruginosa* and *A. baumannii*).

Conflicts of interest

There are no conflicts to declare.

Acknowledgements

PSV thanks the Department of Science and Technology – Science and Engineering Research Board (DST – SERB, YSS/2015/000632) and University Grants Commission (UGC – contract no. MRP-7036/16SERO/UGC) for their financial assistance. PSV also would like to thank the Management of the College for the financial support to establish a laboratory for Nanomaterials.

References

1 S. Sun and W. Wang, *RSC Adv.*, 2014, **4**, 47136–47152.
2 E. Baldev, D. MubarakAli, A. Ilavarasi, D. Pandiaraj, K. A. S. S. Ishack and N. Thajuddin, *Colloids Surf., B*, 2013, **105**, 207–214.
3 J. P. Deebasree, V. Maheskumar and B. Vidhya, *Ultrason. Sonochem.*, 2018, **45**, 123–132.
4 E. Shahriari, M. Moradi and M. Raeisi, *J. Theor. Appl. Phys.*, 2016, **10**, 259–263.
5 I. Khan, K. Saeed and I. Khan, *Arabian J. Chem.*, 2019, **12**, 908–931.
6 A. Azam, A. S. Ahmed, M. Oves, M. S. Khan, S. S. Habib and A. Memic, *Int. J. Nanomed.*, 2012, **7**, 6003–6009.
7 C. Ray and T. Pal, *J. Mater. Chem. A*, 2017, **5**, 9465–9487.
8 P. C. Maness, S. Smolinski, D. M. Blake, Z. Huang, E. J. Wolfrum and W. A. Jacoby, *Appl. Environ. Microbiol.*, 1999, **65**, 4094–4098.
9 K. Nakata and A. Fujishima, *J. Photochem. Photobiol., C*, 2012, **13**, 169–189.
10 Y. Sang, Z. Zhao, M. Zhao, P. Hao, Y. Leng and H. Liu, *Adv. Mater.*, 2015, **27**, 363–369.
11 J. M. Lee, J. H. Baek, T. M. Gill, X. Shi, S. Lee, I. S. Cho, H. S. Jung and X. Zheng, *J. Mater. Chem. A*, 2019, **7**, 9019–9024.
12 Y. Li, J. Zhu, H. Chu, J. Wei, F. Liu, M. Lv, J. Tang, B. Zhang, J. Yao, Z. Huo, L. Hu and S. Dai, *Sci. China: Chem.*, 2015, **58**, 1489–1493.
13 K. Pingmuang, J. Chen, W. Kangwansupamonkon, G. G. Wallace, S. Phanichphant and A. Nattestad, *Sci. Rep.*, 2017, **7**, 1–11.
14 C. Regmi, Y. K. Kshetri, S. K. Ray, R. P. Pandey and S. W. Lee, *Appl. Surf. Sci.*, 2017, **392**, 61–70.
15 A. Y. Booshehri, S. Chun-Kiat Goh, J. Hong, R. Jiang and R. Xu, *J. Mater. Chem. A*, 2014, **2**, 6209–6217.
16 Z. Xiang, Y. Wang, P. Ju, Y. Long and D. Zhang, *J. Alloys Compd.*, 2017, **721**, 622–627.
17 Z. Xiang, Y. Wang, Z. Yang and D. Zhang, *J. Alloys Compd.*, 2019, **776**, 266–275.
18 S. Tokunaga, H. Kato and A. Kudo, *Chem. Mater.*, 2001, **13**, 4624–4628.
19 Y. Wang, Y. Long and D. Zhang, *J. Taiwan Inst. Chem. Eng.*, 2016, **68**, 387–395.
20 U. Lamdab, K. Wetchakun, S. Phanichphant, W. Kangwansupamonkon and N. Wetchakun, *J. Mater. Sci.*, 2015, **50**, 5788–5798.
21 R. L. Frost, D. A. Henry, M. L. Weier and W. Martens, *J. Raman Spectrosc.*, 2006, **37**, 722–732.
22 A. R. Lim, S. H. Choh and M. S. Jang, *J. Phys.: Condens. Matter*, 1995, **7**, 7309–7323.
23 M. M. Sajid, N. Amin, N. A. Shad, S. B. khan, Y. Javed and Z. Zhang, *Materials Science & Engineering B: Solid-State Materials for Advanced Technology*, 2019, **242**, 83–89.
24 P. Longchin, P. Pookmanee, S. Satienperakul, S. Sangsrichan, R. Puntharod, V. Kruefu,

W. Kangwansupamonkon and S. Phanichphant, *Integr. Ferroelectr.*, 2016, **175**, 18–24.
25 W. Zhu, F. Sun, R. Goei and Y. Zhou, *Appl. Catal., B*, 2017, **207**, 93–102.
26 Q. Liang, M. Zhang, C. Yao, C. Liu, S. Xu and Z. Li, *J. Photochem. Photobiol., A*, 2017, **332**, 357–363.
27 G. P. Nagabhushana, G. Nagaraju and G. T. Chandrappa, *J. Mater. Chem. A*, 2013, **1**, 388–394.
28 Y. Wan, S. Wang, W. Luo and L. Zhao, *Int. J. Photoenergy*, 2012, **2012**, 26–28.
29 I. D. Brown and R. D. Shannon, *Acta Crystallogr., Sect. A: Cryst. Phys., Diffr., Theor. Gen. Crystallogr.*, 1973, **29**, 266–282.
30 S. R. M. Thalluri, C. Martinez-Suarez, A. Virga, N. Russo and G. Saracco, *Int. J. Chem. Eng. Appl.*, 2013, **4**, 305–309.
31 M. M. Sajid, S. B. Khan, N. A. Shad and N. Amin, *RSC Adv.*, 2018, **8**, 35403–35412.
32 S. S. Patil, M. G. Mali, M. A. Hassan, D. R. Patil, S. S. Kolekar and S. W. Ryu, *Sci. Rep.*, 2017, **7**, 1–12.
33 A. Arshad, J. Iqbal, M. Siddiq, Q. Mansoor, M. Ismail, F. Mehmood, M. Ajmal and Z. Abid, *J. Appl. Phys.*, 2017, **121**, 024901.
34 V. A. Online, C. Yang, W. Dong, G. Cui, Y. Zhao, X. Shi, X. Xia, B. Tang and W. Wang, *RSC Adv.*, 2017, (7), 23699–23708.
35 Z. Zhang, Y. Ma, X. Bu, Q. Wu, Z. Hang, Z. Dong and X. Wu, *Sci. Rep.*, 2018, **8**, 1–11.
36 M. Mahanthappa, N. Kottam and S. Yellappa, *Appl. Surf. Sci.*, 2019, **475**, 828–838.
37 N. Xuan Sang, N. Minh Quan, N. Huu Tho, N. Tri Tuan and T. Thanh Tung, *Semicond. Sci. Technol.*, 2018, **34**, 025013.
38 S. Marković, A. Stanković, J. Dostanić, L. Veselinović, L. Mančić, S. D. Škapin, G. Dražič, I. Janković-Častvan and D. Uskoković, *RSC Adv.*, 2017, **7**, 42725–42737.
39 M. M. Mohamed, W. A. Bayoumy, M. E. Goher, M. H. Abdo and T. Y. Mansour El-Ashkar, *Appl. Surf. Sci.*, 2017, **412**, 668–682.
40 Y. Li, J. Zhan, L. Huang, H. Xu, H. Li, R. Zhang and S. Wu, *RSC Adv.*, 2014, **4**, 11831–11839.
41 Y. Feng, N. Feng, Y. Wei and G. Zhang, *RSC Adv.*, 2014, **4**, 7933–7943.
42 A. Mai-Prochnow, M. Clauson, J. Hong and A. B. Murphy, *Sci. Rep.*, 2016, **6**, 1–11.
43 H. Wang, J. Wang, P. Yu, P. Ge, Y. Jiang, R. Xu, R. Chen and X. Liu, *Int. J. Mol. Med.*, 2017, **39**, 364–372.
44 K. Gold, B. Slay, M. Knackstedt and A. K. Gaharwar, *Adv. Ther.*, 2018, **1**, 1700033.
45 M. A. Subhan, T. Ahmed, N. Uddin, A. K. Azad and K. Begum, *Spectrochim. Acta, Part A*, 2015, **136**, 824–831.
46 M. A. Subhan, N. Uddin, P. Sarker, H. Nakata and R. Makioka, *Spectrochim. Acta, Part A*, 2015, **151**, 56–63.
47 M. Elango, M. Deepa, R. Subramanian and G. Saraswathy, *Mater. Chem. Phys.*, 2018, **216**, 305–315.

